Rheological and Low Field NMR Characterisation of Cystic Fibrosis Patient's Sputum

G. Staltari,[a] A. Biasin,[a] L. Grassi,[a] F. Gerin,[b] M. Maschio,[c] M. Confalonieri,[d] G. Grassi,[b] M. Grassi,[a] and M. Abrami[a,*]

[a]Department of Engineering and Architecture, University of Trieste, Via Valerio 6/A, I-34127 Trieste, Italy

[b]Department of Life Sciences, Cattinara University Hospital, Trieste University, Strada di Fiume 447, I-34149 Trieste, Italy

[c]Institute for Maternal and Child Health, IRCCS Burlo Garofolo, Via Dell'Istria, 65, I-34137, Trieste, Italy

[d]Cattinara University Hospital, Pulmonology Department, Strada di Fiume 447, I-34149, Trieste, Italy

doi: https://doi.org/10.15255/CABEQ.2022.2119

Original scientific paper
Received: July 8, 2022
Accepted: November 21, 2022

The shear modulus G of the sputum obtained by expectoration from cystic fibrosis patients is fundamental to determine the mesh size of the polymeric network pervading the sputum, a parameter related to lung functionality. The Akaike criterion revealed that in 55.2 % of the examined samples, the best approach (among those considered) to determine G relied on the mechanical spectrum fitting by the generalised Maxwell model with relaxation times scaled by a factor 10. Thus, this approach was adopted to evaluate the mesh size distribution combining G knowledge with the determination of the average magnetic relaxation time (T_{2m}) of sputum. As G and T_{2m} determination can be negatively affected by sputum contamination by saliva, whose presence increases T_{2m} and depresses G, we developed a proper "decontamination" procedure to obtain more reliable T_{2m} and G estimations (necessary in 21 % of the samples). This procedure allowed to strengthen the T_{2m} correlation with lung functionality evaluated by FEV_1 (normalised air volume emitted in the first second during a spirometry test).

Keywords:
rheology, low field NMR, cystic fibrosis, shear modulus, mesh size, saliva contamination

Introduction

The walls of the bronchial tree are covered in a thin aqueous layer, the periciliary layer (PCL), the thickness of which is about 5–10 mm in healthy subjects[1]. Inside PCL, cells cilia beat with a typical frequency of 20 Hz and amplitude of about 5 μm. PCL is coated with another layer, named mucus layer (ML)[2], the thickness of which is about 25–30 μm in healthy subjects. Together, PCL and ML constitute the airway surface layer (ASL)[3] (see Fig. 1). While ML traps inhaled particles and transports them out of the lung by cilia-generated forces, PCL provides a favourable environment for ciliary beating and cell-surface lubrication[4]. The most abundant ML solid component is represented by mucins (1–5 %), a family of high molecular weight, heavily glycosylated proteins containing hydrophobic polypeptide backbones connected to multiple hydrophilic oligosaccharide chains[5]. Besides mucin, other bio-macromolecules, such as proteins, antibodies, and lipids are present inside ML, and they can form a mesh-like structure through disulphide cross-linkages and/or physical entanglements, so that ML shows viscoelastic gel–like properties[6]. Notably, the ASL "gel-on-brush" model[4] also points out that PCL is not a "simple" liquid phase as commonly believed. Indeed, PCL hosts membrane-spanning mucins and large muco-polysaccharides that are tethered to cilia, microvilli, and epithelial surface. All these polymers form a three-dimensional network impeding the ML mucins and inhaled particles to penetrate the PCL environment.

Cystic fibrosis (CF) depends on the dysfunction of the CF transmembrane conductance regulator (CFTR), a channel protein expressed on the membrane of cells, ruling water and ions (Na^+, Cl^-) exchange[7]. This leads to formation of viscous, dehydrated mucoid secretions, in particular in the airways[8], characterised by a pathological increase in proteins, mucin, and biological polymers concentration[9], that consistently reduces the cilia beating efficiency (Fig. 1). The subsequent ML stasis promotes

*Corresponding author: E-mail: michela.abrami@dia.units.it

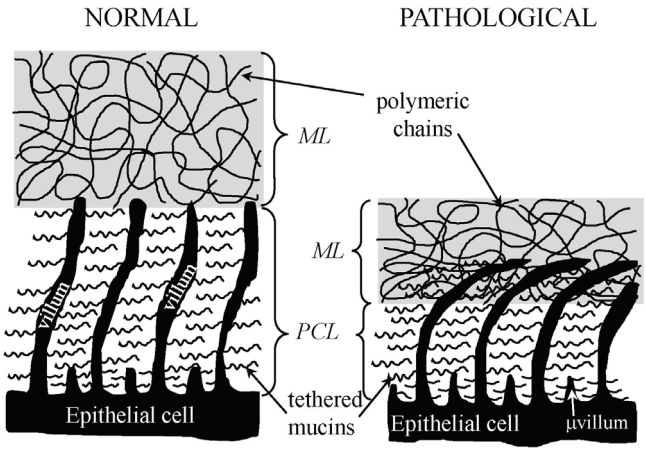

Fig. 1 – *Airway surface layer (ASL) is composed of the mucus layer (ML) and the periciliary layer (PCL). Both ML and PCL contain polymeric substances so that they show a viscoelastic behaviour. In pathological conditions, the dehydrated ML penetrates the PCL so that cilia beating is hindered and ML removal becomes very slow if not impossible. Adapted from ref. 4.*

bacterial infection and inflammation[10], may progress to respiratory failure, the most common cause of death for CF patients[11].

As the increase of ML viscoelasticity correlates to the severity of lung pathology[9, 12] and to the efficacy of drug (mucolytics, anti-inflammatory and antibiotics) released by inhalation (drug diffusivity depends on the ML polymeric network mesh size)[13], the necessity of ML characterisation is of paramount importance from a clinical point of view[14]. Due to the complexity of obtaining direct access to ML, typically, expectorated sputum is considered a surrogate, as it can be easily obtained from patients, and its properties mirror those of ML[9,15].

Among the different available techniques, rheology and low field nuclear magnetic resonance (LF-NMR) have proven very useful for sputum characterisation[14]. Indeed, changes in the rheological properties of mucus/sputum may greatly affect its ability to function as a lubricant, selective barrier, and the body's first line of defence against infection. In addition, the rheological characterisation can provide insight into the nanostructure of a gel-like material such as mucus/sputum. Indeed, as discussed further herein, rheology allows the determination of the mucus/sputum shear modulus that, according to the Flory theory[16], is directly connected to crosslink density, in turn, connected to the polymeric network average mesh size via the equivalent network theory[17]. LF-NMR relies on the ability of hydrogen atoms dipole to react to the perturbation of an external constant magnetic field B_0, where they are embedded. Indeed, inside B_0, hydrogen atoms dipoles tend to line up in the B_0 direction so that, globally, they give origin to the induced magnetisation vector M_v, oriented in the B_0 direction (Z). Due to B_0 perturbation, realised by the application of a proper radio frequency pulse B_1 perpendicular to B_0, M_v rotates in the XY plane of B_1 (that perpendicular to B_0). Upon B_1 removal, M_v tends to line up again into the B_0 direction (relaxation) so that its XY component (M_{vXY}) diminishes with time, and its component in the B_0 direction (conventionally the vertical or Z one; M_{vZ}) increases in time. Interestingly, the relaxation process is affected by the three-dimensional structure embedding the hydrogen atoms, so that it can provide important information about the structure itself. Indeed, interactions with solid surfaces (for instance, dispersed/solubilised polymeric chains) are one of the most important causes affecting the magnetic relaxation of hydrogens. In fact, the relaxation process of water hydrogens near the solid surface (bound water protons) is faster (fast relaxation) than that (slow relaxation) of bulk water protons (free water protons) that are unaffected by solid surface[18]. Accordingly, the average relaxation time (T_{2m}) of hydrogens will depend on the ratio between the solid surface area (S), proportional to the number of protons close to S, and system volume (V), proportional to the total number of protons belonging to the system, as demonstrated by Brownstein and Tarr[19]. In addition, the Scherer theory[20] clearly states that different spatial organisations (cubical, tetrahedral, octahedral) of a polymeric network, reflecting in different S/V ratio, implies different T_{2m} values.

The first aim of this paper was to determine the mesh size distribution of sputum recurring to the theoretical interpretation of rheological and LF-NMR data relative to CF patient sputum. The second aim was to evaluate the effect of possible sputum contamination by saliva on sputum macro- and nano-properties. Indeed, mesh size distribution is related to lung functionality, being small mesh size typically associated to pathological conditions. In addition, in order to improve the efficacy of the drugs usually applied in CF therapy (e.g., mucolytics, anti-inflammatory and antibiotics), an in-depth understanding of the mucus nanostructure is of utmost importance, as drug diffusivity inside a gel-like system depends on the ratio between the diffusing drug molecule radius and the mesh size of the network.

Materials and methods

Samples

The sputum samples represent a subset of those considered by Abrami and co-workers[13]. Briefly, sputum samples were provided by the Burlo Garofolo Hospital, following a procedure approved by the Ethics Committee (prot. no. 496/2916, CI M-11, 22–3-2016). Written informed consent was obtained

from each patient. Spontaneously expectorated (1–2 cm^3) sputum was collected from CF patients in sterile cups, and immediately used for T_{2m} determination and, then, for the rheological characterisation (37 °C) (Haake Mars III Rheometer, GmbH, Karlsruhe, Germany; cone-plate geometry (C35, diameter = 35 mm)).

Rheological characterisation

The mechanical spectrum (elastic (*G*') and viscous (*G*'') moduli dependence on the solicitation pulsation $\omega = 2\pi f$ (in which *f* is the solicitation frequency)) of each sample collected by Abrami and co-workers[13] was interpreted according the generalised Maxwell model (parallel of Maxwell elements, each one constituted by a spring and a dashpot in series) and Voigt model (series of Voigt elements, each one constituted by a spring and a dashpot in parallel)[21].

Generalised Maxwell model in the frequency domain

$$G' = g_e + \sum_{i=1}^{n_R} g_i \frac{(\lambda_i \omega)^2}{1+(\lambda_i \omega)^2} \quad (1)$$

$$G'' = \sum_{i=1}^{n_R} g_i \frac{(\lambda_i \omega)^2}{1+(\lambda_i \omega)^2} \quad (2)$$

where n_R is the number of Maxwell elements considered, whereas g_i (ith elastic constant) and λ_i (ith relaxation time) are model fitting parameters representing the spring constant (g_i) and the relaxation time (λ_i) of the ith Maxwell element. g_e represents the spring constant of the last (n_R + 1) Maxwell element considered purely elastic, i.e. deprived by the dashpot. The simultaneous Eqs.(1)-(2) fitting to experimental data was performed according to two different strategies. The first one assumed that λ_i were scaled by a factor 10 ($\lambda_{i+1} = 10\lambda_i$) while the second assumed that λ_i were allowed to freely vary. In both cases, data fitting was performed minimising the χ^2 statistic:

$$\chi^2 = \sum_{j=1}^{M} \left(\frac{G'_{expj} - G'_j}{G'_{expj}} \right)^2 + \sum_{j=1}^{M} \left(\frac{G''_{expj} - G''_j}{G''_{expj}} \right)^2 \quad (3)$$

where *M* is the number of experimental data, G'_{expj} and G'_j are, respectively, the experimental and the model predicted (Eq.(1)) elastic moduli while G''_{expj} and G''_j are, respectively, the experimental and the model predicted (Eq.(2)) viscous moduli. The determination of n_R was performed according to a statistical procedure[22] aimed at the minimisation of the product $M \cdot \chi^2$, while the sample shear modulus *G* was evaluated as the sum of all the spring constants[23]:

$$(G = g_e + \Sigma_i g_i). \quad (4)$$

Generalised Voigt model in the frequency domain

In order to establish a direct connection between the generalised Maxwell model and the generalised Voigt model, it was necessary to add a Maxwell element (of spring constant g_M and relaxation time λ_M) in series with n_R Voigt elements:

$$J' = \frac{1}{g_M} + \sum_{i=1}^{n_R} \frac{1/g_i}{1+(\lambda_i \omega)^2} \quad (5)$$

$$J'' = \frac{1}{g_M \lambda_M \omega} + \sum_{i=1}^{n_R} \frac{\lambda_i \omega / g_i}{1+(\lambda_i \omega)^2} \quad (6)$$

where *J*' and *J*'' are, respectively, the elastic and viscous compliance, while g_i and λ_i are, respectively, the spring constants and the retardation times of the ith Voigt element. Remembering[21] the relations among *G*', *G*'' and *J*', *J*'':

$$J' = \frac{G'}{(G')^2 + (G'')^2} \quad (7)$$

$$J'' = \frac{G''}{(G')^2 + (G'')^2} \quad (8)$$

and looking at Eq.(1) and (2), the following relation holds:

$$g_M = g_e + \sum_{i=1}^{n_R} g_i \quad \text{in the limit } \omega \to \infty \quad (9)$$

The simultaneous Eqs.(5)-(6) fitting to experimental data was performed assuming that λ_i were scaled by a factor 10 ($\lambda_{i+1} = 10\lambda_i$). Data fitting implied the minimisation of the χ^2 statistic evaluated according to Eq.(2) where G'_{expj} and G''_{expj} were replaced by the corresponding J'_{expj} and J''_{expj} according to Eqs.(7) and (8). The determination of n_R was performed following to the same strategy adopted in the case of the generalised Maxwell model (minimisation of the product $M \cdot \chi^2$) [22]. The shear modulus was evaluated as $G = g_M$.

Mesh size evaluation

Relying on the *G* knowledge, Flory theory[16] allows to evaluate the polymeric network crosslink density, ρ_x, defined as the moles of junction points between different polymeric chains per hydrogel unit volume:

$$\rho_X = G/RT \quad (10)$$

where *R* is the universal gas constant and *T* is the absolute temperature. The reason for *R* presence in Eq. (10) is due to the formal thermodynamic analogy existing between the determination of the retraction force of an ideal rubber and the determination of pressure in an ideal gas[16]. Finally, the equivalent network theory[17] enables the determination of the average mesh size ξ_a of the network:

$$\xi_a = \sqrt[3]{6/(\pi \rho_x N_A)} \quad (11)$$

where N_A is the Avogadro number.

LF-NMR characterisation

The mathematical description of the relaxation process (i.e. the M_{vXY} time reduction) is given by the solution of the magnetization diffusion equation proposed by Brownstein and Tarr[18,19]:

$$I(t) = \sum_{i=1}^{m} A_i e^{(-t/T_{2i})} \quad (12)$$

where t is time, $I(t)$ is the ratio between the time-dependent value of M_{vXY} and its maximum value (M_{vXYmax}) occurring just after B_1 removal, T_{2i} represents the ith spin-spin or transverse relaxation times, while A_i are "weights" proportional to the number of hydrogen atoms whose dipoles relaxation is characterised by T_{2i}. Obviously, we could have also recorded the relaxation process of the magnetisation vertical component of M_v (M_{vZ}, oriented in the conventional B_0 direction), so that the focus would have been on the determination of the spin-lattice relaxation time (T_1). Although both T_2 and T_1 give similar information about the spatial organisation of the polymeric network pervading the sputum (see Introduction), we preferred to consider T_2, since its experimental determination is considerably faster.

Eq. (12) simply states that the relaxation process is the result of "m" exponential relaxation processes, each one characterised by its own relaxation time (T_{2i}) and weight (A_i). The determination of the unknown couples (T_{2i}, A_i) was performed by fitting Eq. (12) to the experimental $I(t)$ values ($I_s(t)$) and the number, m, of exponential decays appearing in Eq. (12) was determined per the statistics applied in the Rheology section[22].

The average magnetic relaxation time (T_{2m}) and the average inverse magnetic relaxation time ($(1/T_2)_m$), depending on several variables such as temperature, B_0 strength, and the presence of a disperse phase in the system as it happens in hydrogel system[18], can be defined by:

$$T_{2m} = \sum_{i=1}^{m} A_i T_{2i} / \sum_{i=1}^{m} A_i \quad \left(\frac{1}{T_2}\right)_m = \sum_{i=1}^{m} \frac{A_i}{T_{2i}} / \sum_{i=1}^{m} A_i$$
$$A_{i\%} = 100 A_i / \sum_{i=1}^{m} A_i \quad (13)$$

While Eq.(12) provides the discrete relaxation time distribution represented by the m couples ($A_{i\%} - T_{2i}$), it is possible to determine the continuous distribution according to Whittal and MacKay[24]:

$$I(t) = \int_{T_{2min}}^{T_{2max}} a(T_2) \exp\left\{-\frac{t}{T_2}\right\} dT_2 \quad (14)$$

where T_{2max} (= 10^4 ms) and T_{2min} (= 1 ms) indicate, respectively, the lower and upper values of the continuous T_2 distribution, $a(T_2)$ is the unknown amplitude of the spectral component at the relaxation time T_2 while $\exp\{-t/T_2\}$ represents the decay term. Eq.(14) represents the "continuous" expression of Eq.(12). This means that while Eq.(12) describes the M_{vXY} relaxation process by means of a limited (discrete) number of initially unknowns T_{2i}, Eq.(14) makes use of a much higher number of known relaxation times belonging to the interval ($T_{2min} - T_{2max}$) and comprehending all the possible relaxation times characterising the sample under study (continuous distribution of relaxation times).

In order to fit the experimental M_{vXY} time decay ($I_s(t)$) by Eq.(14), and obtain the continuous T_2 distribution (the unknowns $A_i = a_i(T_{2i}) \cdot \Delta T_{2i}$), the following discretisation was applied[24]:

$$I(t) \approx \sum_{i=1}^{N} a_i e^{\left\{-\frac{t}{T_{2i}}\right\}} (T_{2i+1} - T_{2i}) = \sum_{i=1}^{N} A_i e^{\left\{-\frac{t}{T_{2i}}\right\}} \quad (15)$$

where the range of the T_2 distribution ($T_{2min} - T_{2max}$) was logarithmically subdivided into N = 200 parts (higher N values were unnecessary). Because of the noise disturbing the measure of I_s, the fitting procedure must not minimise the χ^2 statistic, but a smoothed definition[24] of it (χ_s^2):

$$\chi_s^2 = \sum_{i=1}^{N} \left(\frac{I_s(t_i) - I(t_i)}{\sigma_i} \right)^2 + \mu \sum_{i=1}^{N-2} \left| A_{i+2} - 2A_{i+1} + A_i \right|^2 \quad (16)$$

where σ_i is the ith datum standard deviation, μ is the weight of the smoothing term (second summation in Eq. (16)) proposed by Provencher[25]. Although different criteria can be used to determine μ, the strategy proposed by Wang[26] was applied. Based on this strategy, the correct μ value is that occurring just below the heel (slope variation) of the function $\ln(\chi_s)$ vs $\ln(\mu)$. In this work, μ = 150 was determined.

The discrete and continuous T_2 distribution can be transformed into hydrogel mesh size distribution resorting to one of the fundamental relations of the low-field NMR field. This relation, based on the solution of the magnetisation diffusion equation proposed by Brownstein and Tarr[18,19], establishes the link between $(1/T_2)_m$ and the ratio of the surface (S) of the dispersed/solubilised substances in the sample and the volume (V) of the sample water molecules:

$$\left(\frac{1}{T_2}\right)_m = \frac{1}{T_{2H_2O}} + \frac{S}{V} M \quad (17)$$

where T_{2H_2O} is the bulk protons relaxation time (i.e. the water proton relaxation time in the absence of polymer, the so-called free water relaxation time ≈ 3700 ms at 37 °C and B_0 = 0.47 T [27]) and M (length/time) is a physical parameter, named relaxivity, representing the effect of the polymer chains surface on water protons relaxation. Indeed, M is equal to the ratio between thickness and relaxation time of the bound water layer adhering to the solid surface.

Eq.(17), stating that $(1/T_2)_m$ depends on (S/V), clearly establishes the relation between the relaxation time and the spatial organisation of the sample network that heavily affects the S/V ratio[18]. Usually, in many polymeric solutions, crosslinking induces a spatial reorganisation of the polymeric chains contained in the original solution that involves the increase of the ratio S/V[28,29]. This, in turn, reflects in the increase of $(1/T_2)_m$ and in the decrease of T_{2m}.

Despite its theoretical importance, Eq.(17) can be re-written in a more useful form, based on the Fiber-Cell[18] and Scherer[20] theories. For this purpose Abrami *et al.*[30] demonstrated that, for a hydrogel polymer volume fraction $\phi < 0.6$, the term (S/V) can be expressed as a function of the average mesh size ξ_a of the polymeric network (error < 5 % with respect to the Scherer theory[20]):

$$\frac{S}{V} = \frac{2}{\xi_a \sqrt{\frac{C_0}{C_1}\frac{1-0.58\varphi}{\varphi}}} \tag{18}$$

where C_0 and C_1 are two constants depending on the mesh architecture and equal, respectively, to 1 and 3π in the case of cubic mesh[20]. In the light of Eq. (18), Eq.(17) becomes:

$$\left(\frac{1}{T_2}\right)_m = \frac{1}{T_{2H_2O}} + 2\frac{M}{\xi_a \sqrt{\frac{C_0}{C_1}\frac{1-0.58\varphi}{\varphi}}} \tag{19}$$

While Eq.(19) refers, averagely, to all the polymeric network meshes, similar expressions can be written for meshes of different dimensions (ξ_i), assuming the M independence on the mesh size[18]:

$$\frac{1}{T_{2i}} = \frac{1}{T_{2H_2O}} + 2\frac{M}{\xi_i \sqrt{\frac{C_0}{C_1}\frac{1-0.58\varphi}{\varphi}}} \tag{20}$$

where T_{2i} is the relaxation time of water protons trapped in polymer meshes of size ξ_i. The bi-univocal correspondence between T_{2i} and ξ_i holds solely in the fast-diffusion regime (typical of gels), i.e when the mobility of water molecules, expressed by their self-diffusion coefficient D ($3.04 \cdot 10^{-9}$ m^2 s^{-1} at 37 °C [31]), is large whether compared to the rate of magnetisation loss ($R_c \cdot M$) (i.e., $R_c \cdot M/D \ll 1$). In the slow diffusion regime, relaxation of all the water protons contained in the volume of a mesh of size ξ_i is not described by only one T_{2i} but several T_{2i}. R_c, indicates the radial distance from the polymer chain axis where the effect of polymeric chains on water proton relaxation becomes negligible. This can be expressed by[18]:

$$R_c = \frac{r_f}{\sqrt{\varphi}} \tag{21}$$

The combination of Eqs.(19) and (20) allows to conclude that the ratio between ξ_i and its average value, ξ_a, depends exclusively on the relaxation times T_{2i} and T_{2m} (except for the free water relaxation time T_{2H_2O}):

$$\xi = \xi_a \frac{\left(\left(\frac{1}{T_2}\right)_m - \frac{1}{T_{2H_2O}}\right)}{\left(\frac{1}{T_{2i}} - \frac{1}{T_{2H_2O}}\right)} \tag{22}$$

Thus, Eq.(12) or Eq.(15) fitting to experimental M_{vXY} decay ($I_s(t)$) allows determining the discrete or continuous relaxation spectrum ($A_{i\%} - T_{2i}$), whereas Eq.(22) allows the conversion of the time relaxation spectrum into the mesh size relaxation spectrum ($A_{i\%} - \xi_i$).

LF-NMR measurements were performed at 37 °C by means of a Bruker Minispec mq20 (0.47 T, Germany). The determination of T_{2m} was performed according to the CPMG sequence (Carr–Purcell–Meiboom–Gill)[32] {90°[-τ-180°-τ(echo)]n-T_R} with a 8.36 μs wide 90°pulse, τ = 250 μs, and T_R (sequences repetition rate) equal to 10 s. In order to obtain the final I_s of 2 %, the proper n was chosen. m was determined according to the statistics applied in the Rheology section[22]. Each spin-echo decay, composed by n points, was repeated 36 times (number of scans).

Statistical analysis

The nature of the experimental data distribution (normal or not) was evaluated by the Kolmogorov-Smirnov test (KS-test). Based on KS-test results, the Spearman's correlation coefficient (r_{sp}) was considered to verify possible direct or inverse correlations among variables. Correlations among variables were considered significant when $p < 0.05$ (i.e. a probability of 95 %). Lower probability was associated to a lack of correlation among variables.

Results and discussion

As previously discussed, the role played by the shear modulus G on the determination of the discrete and the continuous mesh size distribution is very important. Indeed, it serves for the estimation of the average network mesh size ξ_a (Eqs.(10)–(11)) around which LF-NMR information allow to build up the whole mesh size distribution (Eq.(22)). G evaluation, in turn, implies the determination of the mechanical relaxation spectrum, a topic that has been long discussed and debated in literature and that was matched according to different and interesting strategies[33–39]. As a detailed analysis of all these strategies is outside the scope of this paper,

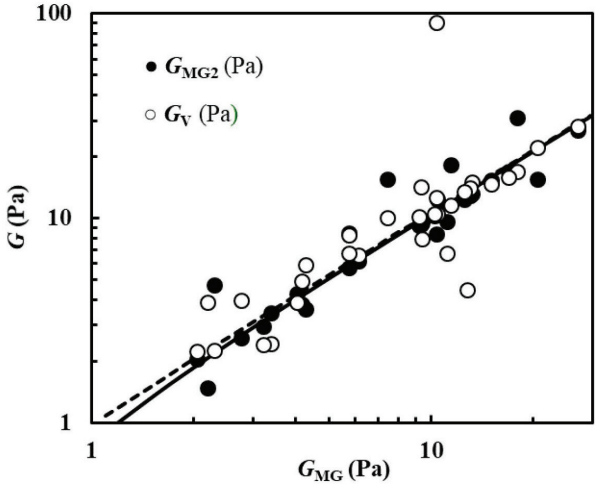

Fig. 2 – *Dependence of the samples shear modulus evaluated according to the MG2 (closed circles; G_{MG2}) and V (open circles; G_V) strategies on the shear modulus estimated according to the MG approach (G_{MG}). Solid and dashed lines indicate the linear interpolants, according to a robust fitting approach, referring to the (G_{MG2} vs G_{MG}) and the (G_V vs G_{MG}) trends.*

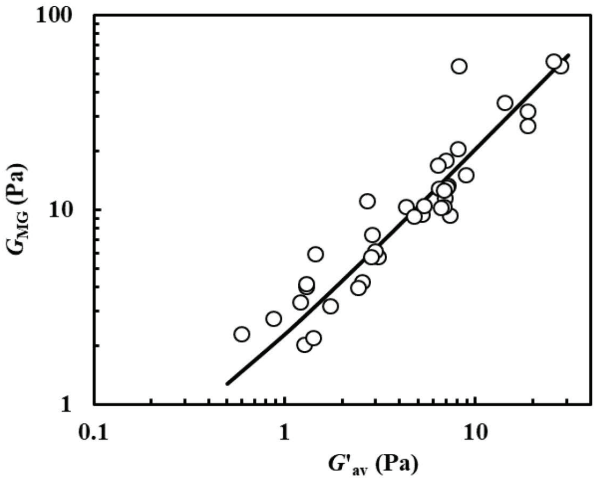

Fig. 3 – *Dependence of the shear modulus evaluated according to the MG strategy (open circles, G_{MG}) and the average value of the elastic modulus (G'_{av}) pertaining to each sample. The solid line represents the linear interpolant evaluated according to a robust fitting approach.*

we focussed the attention on three simple approaches, i.e., those presented in the *Materials and Methods* section (*Generalised Maxwell* and *Voigt models*). In the first two cases, recourse was made to the generalised Maxwell model fitting to mechanical spectrum data assuming relaxation times (λ_i) scaled by a factor "10" (*MG* approach) or freely varying upon data fitting (*MG*2 approach). The last approach refers to the use of the generalised Voigt model fitting to the compliance data *J*' and *J*'' obtained from the *G*' and *G*'' data according to Eqs. (7)–(8) and assuming the retardation times (λ_i) scaled by a factor "10" (*V* approach).

Fig. 2, showing the G_{MG2} and G_V dependence on G_{MG}, reveals that, approximatively, the three approaches lead to similar results as both G_{MG2} and G_V increase with G_{MG} and this linear correlation is statistically significant as proved by the value of the Pearson correlation coefficient (G_{MG2} *vs* G_{MG}: r_{sp} = 0.94 with $p < 10^{-4}$; G_V *vs* G_{MG}: r_{sp} = 0.89 with $p < 10^{-4}$). In addition, the interpolating straight lines reported in Fig. 2 ($G_{MG2} = 1.07 \cdot G_{MG} - 0.27$, solid line; and $G_V = 1.07 \cdot G_{MG} - 0.10$, dashed line), evaluated according to a robust data fitting strategy due to a small data scattering[40], reveal that both the slope (*m*) and the intercept (*q*) are close to 1 and 0, respectively.

In order to explore the physical soundness of the shear moduli evaluated according to the three strategies (G_{MG}, G_{MG2}, G_V), a comparison was performed with the average elastic modulus (G'_{av}), calculated as arithmetic media (on the pulsation range explored) of the experimental *G*' values referring to each sample. Fig. 3, in particular, showing the G_{MG} vs G'_{av} trend (open circles), indicates the existence of a linear correlation (r_{sp} = 0.93, $p < 10^{-4}$) among these physical quantities. In addition, the linear interpolant (robust fitting; $G_{MG} = 2.03 \cdot G'_{av} + 0.26$) reveals that G_{MG} is approximately two times G'_{av} as the line slope is near 2 and the intercept is close to zero. In the case of the other two approaches, we found again the existence of linear correlations with G'_{av} even if characterized by a smaller intensity (*MG*2: r_{sp} = 0.88, $p < 10^{-4}$, $G_{MG} = 2.26 \cdot G'_{av} - 0.46$; *V*: r_{sp} = 0.86, $p < 10^{-4}$, $G_{MG} = 2.27 \cdot G'_{av} - 0.1$. Data not shown) due to a wider data dispersion. A possible way to quantify this last aspect is to consider the dependence of the ratio between the evaluated shear modulus (G_{MG}, G_{MG2} or G_V) and G'_{av} as reported in Fig. 4 for the case of G_{MG}/G'_{av} vs G'_{av}. It can be

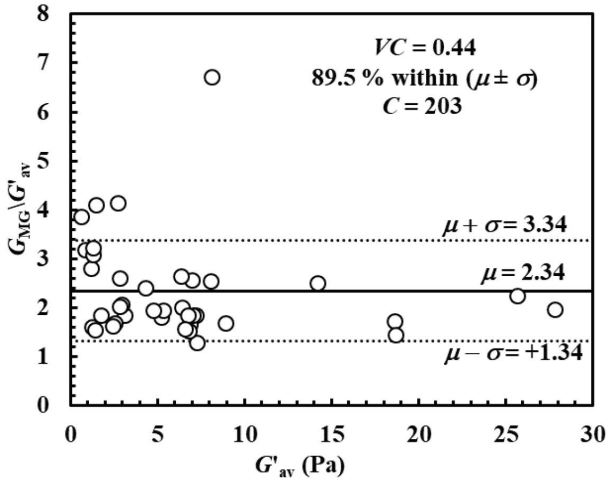

Fig. 4 – *Dependence of the ratio G_{MG}/G'_{av} (open circles) versus G'_{av}. G_{MG} indicates the samples shear modulus evaluated according to the MG strategy while (G'_{av}) is the arithmetic media of the experimental G' values referring to each sample. VC is the variation coefficient (ratio between the average value, μ, and the standard deviation, σ) while C is the ratio between the percentage of data falling within the (μ ± σ) and the standard deviation σ.*

seen that 89.2 % of the data fall within the average value (μ = 2.34) ± one standard deviation (σ = 1.0), the variation coefficient *VC* = 0.44 while the ratio *C* between the data percentage falling within ($\mu \pm \sigma$) and σ is equal to 203. In the case of G_{MG2}/G'_{av} vs G'_{av}, the data percentage falling within ($\mu \pm \sigma$; μ = 2.5, σ = 1.4) decreases to 86.1 %, *VC* increases up to 0.55 and *C* decreases to 156. Finally, for what concerns the case G_V/G'_{av} vs G'_{av}, 100 % of the data fall within ($\mu \pm \sigma$; μ = 3.0, σ = 3.3) as *VC* is very high (1.1) while *C* decreases to 90. Observing the *VC* and *C* values, it follows that, concerning data scattering around μ, the best situation competes to the *MG* strategy (lowest *VC* and biggest *C*). The worst situation is instead related to *V* approach (highest *VC* and lowest *C*) while *MG*2 approaches is in between. However, again, all the three approaches seem to lead to reasonable data as the predicted shear modulus is, correctly, higher than G'_{av} but not so much (≈ between 2 and 3) this suggesting that the experimental window explored should be representative of the sample viscoelastic properties. Should it not be the case, much higher shear modulus estimations would occur as the purely elastic behaviour takes place for $\omega \rightarrow \infty$.

The only criterion that clearly assigns the role of a preferable approach to *MG*, among those considered, is the Akaike criterion (*AIC* number)[41]:

$$AIC = M\ \ln(\frac{\chi^2}{M}) + 2\frac{(N_F+1)M}{M-N_F-2} \qquad (23)$$

where *M* is the number of experimental data, N_F is the number of fitting parameters, and χ^2 is defined by Eq.(3). According to this criterion, the best model is that characterised by the lowest *AIC*. Table 1 showing, for all samples, the values of G_{MG}, G_{MG2} and G_V, reveals that, in the 55.2 % of the cases, the *MG* approach is the one to be preferred, while the percentage goes down to 31.6 % and 13.2 % in the *V* and *MG*2 cases, respectively. In addition, in 2 out 38 samples, the *MG*2 approach cannot provide a statistically (*F*-test) reliable fitting. Thus, the *MG* approach has been considered for the evaluation of average mesh size (ξ_a, Eqs. (10)-(11)) of the polymeric network pervading the sputum samples.

Table 2 shows, for all the samples reported in Table 1, the values of the average relaxation time (T_{2m}), the average inverse relaxation time ($(1/T_2)_m$), the average mesh size (ξ_a), the ith meshes percentage fraction ($A_{i\%}$), the relaxation times (T_{2i}), and the dimensions (ξ_i) calculated for each samples. The combination of the rheological characterisation, enabling the determination of ξ_a, and the LF-NMR one (allowing the evaluation of the discrete relaxation spectrum $A_{i\%} - T_{2i}$), permits the determination of the discrete mesh size distribution ($A_{i\%} - \xi_i$). Table 2 reveals that the relaxation spectrum, and thus, the mesh size distribution, is composed by 2 – 4 contributes, 3 being the most frequent case. Basically, this means that our samples are heterogeneous, since homogeneous systems are characterised only by one relaxation mode ($T_{2m} = T_{21}$)[29,42]. Indeed, it is well known that sputum is a heterogeneous system[13]. In addition, Table 2 shows that T_{2m} spans from about 200 ms to 2000 ms, this being reasonable, as the T_{2m} measured in healthy subjects' sputum (mainly composed of saliva) is around 3000 ms[43]. Regarding the mesh size (ξ_i), we can see from Table 2 that ξ_i ranges between about 10 nm to 1000 nm. As it is known that the polymeric network, pervading CF patients mucus, is organised with an average mesh size which lies in the range (60 – 300) nm[44,45] and that healthy subjects' mucus is characterised by a mesh size approximately ≤ (500–600) nm, we have to conclude that when ξ_i exceeds 600 nm, a probable sputum contamination by saliva could have occurred. Indeed, upon expectoration, it can happen that the exiting mucus, coming from the deeper part of the respiratory tract, mixes with other aqueous liquids (typically saliva) pervading the upper part of the respiratory tract and not related to lungs clinical conditions. Thus, we can say that the sputum has been contaminated by saliva and, consequently, its relaxation time (T_{2m}) is anomalously increased, as saliva is characterised by a high relaxation time (> 2000 ms). In our approach, this reflects in unreasonably high mesh sizes (see Eq. (22)). This is the reason why we proposed a way for the elimination of the effect of possible contamination from saliva (decontamination). For this purpose, we determined the continuous distribution of the relaxation times (Eq. (14)) and, by means of a deconvolution approach[46], the contribute of saliva was eliminated, as explained in the following. The main assumption of our approach relied on the hypothesis that the continuous relaxation distribution can be described by a sum of Weibull equations, as this approach proved to be successful[47]:

$$W(T_2) = \sum_{j=1}^{j=N_w} A_i \left(\frac{2\delta_j}{\eta_j}\right)\left(2\frac{T_2 - T_{2min-j}}{\eta_j}\right)^{\delta_j - 1} \exp\left(-\left(2\frac{T_2 - T_{2min-j}}{\eta_j}\right)^{\delta_j}\right) \qquad (24)$$

where N_w is the number of Weibull equations considered, A_j, d_j, η_j and T_{2min-j} are model fitting parameters. N_w was determined according to the same strategy adopted to obtain n_R (Eqs.(1)-(2)) and *m* (Eq.(12)).

The criterion to decide which samples needed the correction was the existence of $\xi_i \geq 600$ nm or $T_{2i} \geq 2000$ ms (see grey marked samples in Table 2). Let us now focus attention on sample 1 of Table 2, chosen as an example, to explain the decontamination procedure. Fig. 5, showing the continuous relaxation time distribution (open circles) determined by Eq.(15) fitting to experimental data, reveals the presence of two, unresolved, peaks centred, respec-

Table 1 – *Average elastic modulus (G'_{AV}) and shear modulus evaluated according to generalised Maxwell model fitting to mechanical spectrum data (assuming relaxation times λ_i scaled by a factor 10 (G_{MG}) or let to freely change (G_{MG2})), and shear modulus evaluated according to the generalised Voigt model fitting to mechanical spectrum data assuming retardation times λ_i scaled by a factor 10 (G_V). AIC indicates the Akaike number (Eq. (23)).*

#	G'_{AV} (Pa)	G_{MG} (Pa)	*AIC*	G_{MG2} (Pa)	*AIC*	G_V (Pa)	*AIC*
1	3.1	5.7	–171	8.4	–172	8.3	–175
2	3.0	6.1	–110	6.2	–112	6.6	–112
3	1.4	5.9	–96	–	–	14.4	–94
4	2.9	7.4	–169	15.5	–188	10.0	–197
5	5.2	9.4	–75	9.5	–70	7.9	–72
6	2.5	4.3	–81	3.6	–72	5.9	92
7	1.3	2.0	–98	2.0	–95	2.2	–99
8	2.4	4.0	–94	–	–	4.4	–97
9	7.0	18.0	–131	31.0	–118	16.9	–121
10	27.8	54.6	–139	57.2	–143	66.6	–133
11	8.9	15.1	–162	15.3	–159	14.7	–107
12	5.4	10.5	–140	12.3	–139	10.5	–143
13	7.2	13.3	–158	13.2	–153	14.9	–205
14	2.8	5.7	–106	5.7	–100	6.7	–99
15	8.0	20.6	–127	15.4	–93	22.1	–128
16	1.2	3.4	–92	3.5	–76	2.4	–62
17	25.7	57.8	–183	58.1	–190	54.0	–192
18	6.9	11.5	–159	18.2	–131	11.6	–149
19	8.1	54.6	–149	42.1	–143	35.4	–139
20	2.7	11.2	–135	9.6	–131	6.7	–127
21	1.7	3.2	–122	3.0	–114	2.4	–65
22	18.6	32.1	–205	27.4	–213	27.5	–190
23	4.3	10.4	–117	8.3	–109	90.9	99
24	1.4	2.2	–96	1.5	–89	3.9	–84
25	7.3	9.4	–113	9.4	–111	14.1	–112
26	7.0	13.0	–159	12.9	–170	14.1	–167
27	14.2	35.6	–145	30.5	–143	46.6	–148
28	6.4	12.8	–82	13.3	–80	4.5	–67
29	0.6	2.3	–50	4.7	–49	2.3	–42
30	6.8	12.5	–152	12.4	–146	13.4	–149
31	18.7	27.2	–146	27.1	–144	28.2	–163
32	4.8	9.3	–164	9.2	–166	10.2	–153
33	6.4	16.9	–152	16.8	–150	15.9	–153
34	0.9	2.8	–119	2.6	–115	3.9	–103
35	1.3	4.0	–88	4.3	–85	3.9	–85
36	1.3	4.2	–92	3.8	–93	4.9	–92
37	6.8	10.4	–106	10.4	–100	12.6	–95
38	6.6	10.3	–118	10.3	–115	10.5	–100

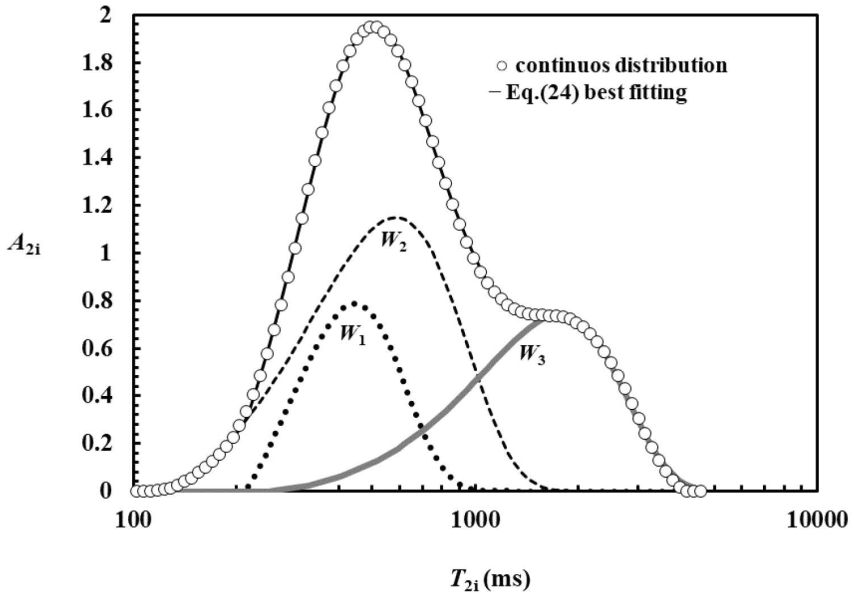

Fig. 5 – *Continuous relaxation distribution (A_{2i} vs T_{2i}; white circles) referring to sample 1 of Tables 1 and 2. The solid black line indicates Eq.(24) best fitting, sum of the three Weibull equations W_1 (dotted line), W_2 (dashed line) and W_3 (solid grey line).*

tively, around 520 ms and 1900 ms. In virtue of their position on the relaxation times scale, it can be argued that the first one represents the magnetic relaxation of the water hydrogens contained inside the polymeric network pervading the sputum, while the second should represent the water outside the polymeric network, i.e. the water fraction experiencing a less intimate contact with the polymeric chains surface *S*. Indeed, Eq.(17) states that the relaxation time of the water hydrogens contained inside the polymeric network is lower than that referring to water hydrogens outside the polymeric network as the ratio S/V (S = polymeric chains surface; V = water volume) is higher inside the network. In other words, inside the network the specific polymeric chains surface ($m^2\,m^{-3}$) in contact with water molecules is higher than outside due to the presence of the network. From this view point, we could suppose that the external water would surround the polymeric network entrapping the inner water. In order to properly fit the continuous relaxation time distribution, three ($N_W = 3$) Weibull equations were needed, as depicted in Fig. 5. Again, observing the position of the three peaks, we can reasonably say that the first two (W_1 and W_2) are connected to the water trapped inside the polymeric network ($T_2 <$ 2000 ms), while the third (W_3) described the water fraction outside the network (≈ 2000 ms). As the left tail of W_3 prolongs up to small relaxation times (about 300 ms), we should conclude that the contour separating the inner and the external water is not sharp and regular. Indeed, this finding suggests that the sputum is not only characterised by a nano-inhomogeneity, accounted for by W_1 and W_2, but also by a micro-inhomogeneity represented by W_3. This ultimately suggests that, upon expectoration, mucus and saliva mix together to give origin to a micro-heterogeneous structure (sputum). Relying on these considerations, it is possible to decontaminate the original relaxation spectrum by simply subtracting the effect of the external water (W_3) to obtain the cleaned relaxation time shown in Fig. 6. On the basis of Eq. (22), the relaxation time distributions (original and decontaminated) can be converted into the mesh distribution reported in Fig. 7. It is interesting to underline that, while the original mesh size distribution extends up to unsound wide meshes (thin line), the decontaminated one (thick line) spans, approximately, in the classical range 20 – 300 nm[48].

The repetition of this strategy for all the contaminated samples (those marked in grey in Table 2) allows to draw an interesting conclusion concerning the relation between T_{2m} and FEV_1, one of the most common markers used in the practical clinic to evaluate lung functionality[49]. Indeed, forced expiratory volume (*FEV*) refers to the volume of air that an individual can exhale during a forced breath in t seconds[50]. Usually indicated as *FEV*, it is followed by a subscript that indicates the number of seconds of the measurement's duration. For instance, forced expiratory volume in 1 second (FEV_1) is the maximum amount of air that the subject can forcibly expel during the first second following maximal inhalation[51]. Although age and gender are the major factors that affect the average values of *FEV* in healthy individuals, height, weight, ethnicity, and decreased patient effort are some of

Table 2 – *Average relaxation time (T_{2m}), average inverse relaxation time ($(1/T_2)_m$), average mesh dimension (ξ_a), i^{th} meshes percentage fraction ($A_{i\%}$), relaxation time (T_{2i}), and dimension (ξ_i) referring to the different samples. Grey marked samples underwent the decontamination procedure.*

#	T_{2m} (ms)	$(1/T_2)_m$ (ms^{-1})	ξ_a (nm)	$A_{i\%}$ (–)	T_{2i} (ms)	ξ_i (nm)
1	861	$1.77\cdot10^{-3}$	110.6	17.5 42.8 39.6	2182.6 797.7 344.5	883.1 168.4 62.9
2	897	$1.49\cdot10^{-3}$	108.7	15.0 52.9 32.2	2190.8 828.5 408.4	716.0 142.1 61.1
3	494	$2.93\cdot10^{-3}$	109.8	20.5 44.6 34.9	1108.0 441.2 201.7	461.4 146.1 62.2
4	308	$4.08\cdot10^{-3}$	101.9	19.4 65.8 14.8	611.8 261.5 118.6	284.6 109.2 47.6
5	1276	$1.28\cdot10^{-3}$	94.1	43.6 41.3 15.1	2095.7 775.6 280.9	459.1 93.1 28.8
6	2130	$5.18\cdot10^{-4}$	122.4	86.0 14.0	2322.5 946.0	189.4 38.5
7	1006.5	$1.38\cdot10^{-3}$	156.8	34.5 43.9 21.6	1655.3 826.2 338.2	521.4 185.0 64.7
8	883	$1.71\cdot10^{-3}$	125.4	38.3 32.4 29.3	1463.6 730.1 292.2	436.8 163.9 57.2
9	303	$4.36\cdot10^{-3}$	75.8	6.9 42.6 50.5	955.6 365.0 161.8	399.7 125.6 52.5
10	393	$4.58\cdot10^{-3}$	52.4	14.1 22.5 45.4 18.0	1224.5 483.2 205.3 100.8	413.2 125.4 49.0 23.4
11	366	$2.91\cdot10^{-3}$	84.4	31.5 68.5	510.8 298.7	132.0 72.4
12	946	$1.37\cdot10^{-3}$	90.9	30.5 60.2 9.3	1632.8 699.4 287.5	292.7 86.3 31.2
13	493	$3.22\cdot10^{-3}$	84.0	24.2 42.6 33.2	1047.2 434.9 165.4	361.9 122.1 42.9
14	1059	$1.66\cdot10^{-3}$	111.2	36.4 33.8 29.8	1923.8 812.3 283.3	618.6 160.4 47.3
15	728	$1.95\cdot10^{-3}$	75.5	32.9 51.6 15.5	1218.0 575.5 197.4	230.9 86.6 26.5
16	559	$2.43\cdot10^{-3}$	132.6	20.0 61.0 19.0	1117.4 492.0 187.3	459.7 162.9 56.6
17	210	$5.20\cdot10^{-3}$	51.4	56.9 43.1	260.7 142.9	71.1 37.7
18	174	$6.65\cdot10^{-3}$	88.2	21.5 78.5	330.0 131.0	203.7 76.3
19	171	$7.01\cdot10^{-3}$	52.4	20.4 79.6	355.6 123.6	139.0 45.2

Table 2 – *continued*

#	T_{2m} (ms)	$(1/T_2)_m$ (ms^{-1})	ξ_a (nm)	$A_{i\%}$ (–)	T_{2i} (ms)	ξ_i (nm)
20	448	$3.90 \cdot 10^{-3}$	88.9	21.5 37.6 40.9	1175.8 352.2 154.3	557.1 125.7 52.0
21	1842	$0.98 \cdot 10^{-3}$	134.9	53.7 29.3 16.9	2780.5 989.4 341.4	1084.0 130.3 36.3
22	482	$2.52 \cdot 10^{-3}$	62.6	22.7 70.9 6.4	866.3 389.3 145.1	159.4 61.3 21.3
23	487	$2.21 \cdot 10^{-3}$	91.2	46.2 53.8	628.3 364.9	133.8 71.6
24	820	$1.99 \cdot 10^{-3}$	152.8	16.7 45.3 32.3 5.7	1831.2 861.3 364.1 116.9	956.3 295.8 106.4 31.8
25	503	$2.42 \cdot 10^{-3}$	94.3	14.7 67.5 17.8	979.2 477.0 207.1	270.5 111.2 44.6
26	351	$3.43 \cdot 10^{-3}$	84.4	40.7 50.8 8.5	502.5 269.8 114.8	155.3 77.7 31.6
27	659	$2.20 \cdot 10^{-3}$	64.4	18.0 47.8 34.2	1539.7 609.1 263.8	327.7 90.5 35.3
28	657	$1.69 \cdot 10^{-3}$	84.9	39.4 60.6	935.3 476.7	151.1 66.0
29	842	$1.40 \cdot 10^{-3}$	150.7	9.5 45.4 45.1	1797.7 968.3 514.1	595.1 223.0 101.5
30	624	$2.49 \cdot 10^{-3}$	85.6	10.5 62.0 27.5	2033.4 571.5 203.7	857.7 128.2 40.9
31	253	$4.73 \cdot 10^{-3}$	66.1	8.4 70.2 21.4	632.0 248.6 120.7	224.7 78.5 36.8
32	368	$3.29 \cdot 10^{-3}$	94.7	17.6 66.0 16.3	667.5 342.0 149.4	232.7 107.7 44.5
33	164	$6.79 \cdot 10^{-3}$	77.4	13.1 52.7 34.2	353.6 133.1 138.8	197.5 69.8 72.9
34	406	$2.82 \cdot 10^{-3}$	141.6	42.8 57.2	581.3 274.7	248.8 107.0
35	401	$2.94 \cdot 10^{-3}$	125.0	18.4 62.6 18.9	679.7 384.4 183.0	277.4 142.9 64.1
36	544	$2.03 \cdot 10^{-3}$	123.6	73.8 26.2	627.4 307.9	164.2 72.9
37	409	$3.46 \cdot 10^{-3}$	92.2	21.1 55.3 23.6	874.9 342.9 146.7	337.5 111.3 45.0
38	730	$2.16 \cdot 10^{-3}$	92.7	32.5 46.0 21.5	1386.3 509.0 211.3	387.5 103.1 39.1

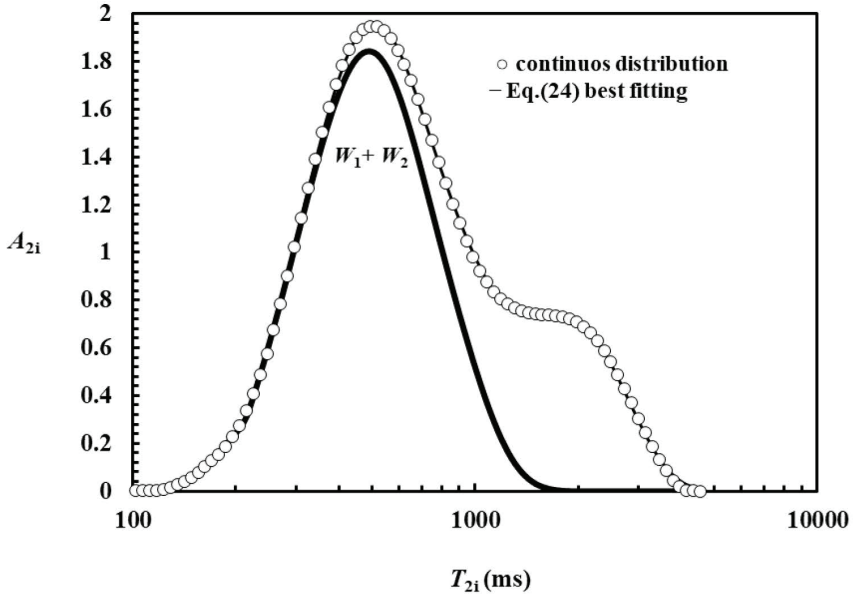

Fig. 6 – *Continuous relaxation distribution (A_{2i} vs T_{2i}; white circles) referring to sample 1 of Tables 1 and 2. The solid thick line represents the cleaned relaxation distribution (sum of W_1 and W_2), deprived by the effect of the external water (W_3).*

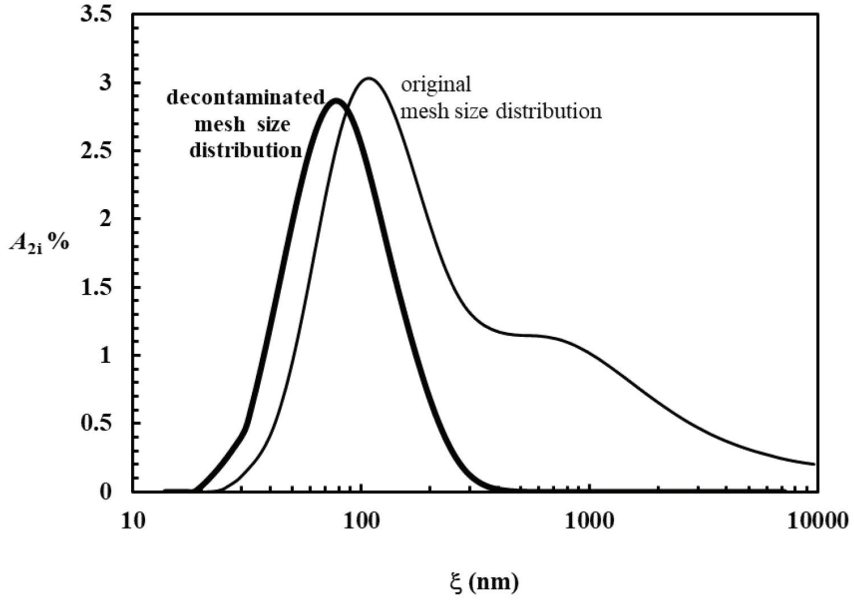

Fig. 7 – *Comparison between the decontaminated (thick line) and the original (thin line) mesh size distribution obtained via Eq.(22) from the time relaxation distribution shown in* Fig. 6 *and referring to sample 1 of Tables 1 and 2. ξ is the mesh dimension.*

the other influencing factors[52,53]. FEV_1 values greater than 80 % of the predicted average value are considered to be normal[54]. Fig. 8 shows the relation existing between T_{2m} and FEV_1 without correction for saliva contamination (open circles) and considering the decontamination (closed circles). It is clear that decontamination allowed reducing data scattering along the interpolating straight line (T_{2m}(ms) = 13.4·FEV_1(–) – 102; decontaminated data), as proved by the Spearman correlation coefficient that increases from 0.4 to 0.62 (p = 0.008) upon T_{2m} data decontamination. Thus, at least partially, the random contamination of saliva can introduce noise in T_{2m} evaluation. Consequently, the decontamination procedure increases significantly the clinical reliability and importance of our LF-NMR approach. In the case of the T_{2m} – G relation, decontamination seems to play a minor role as r_{sp} increases upon decontamination from –0.57 to –0.48 (p < 0.0025). The reason for this result could be the simultaneous

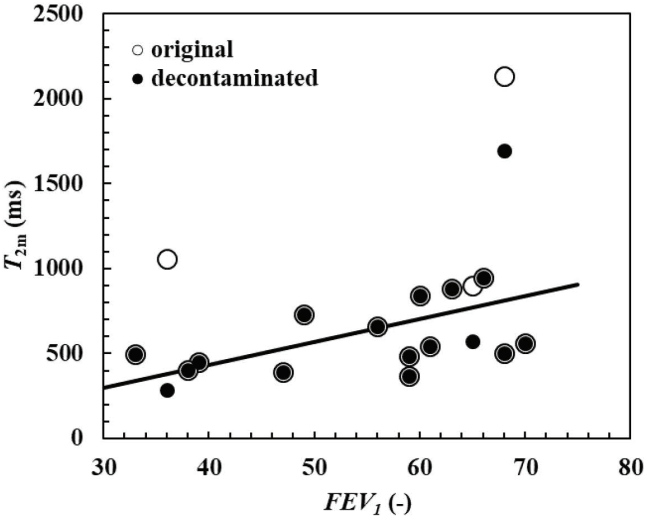

Fig. 8 – *Correlation between the sputum average relaxation time (T_{2m}) and FEV_1 (known for 17 out of 38 samples). Open circles refer to T_{2m} data not corrected for the possible saliva presence (original), while closed circles represent corrected (decontaminated) T_{2m} data. Straight line is the linear interpolant evaluated on corrected data.*

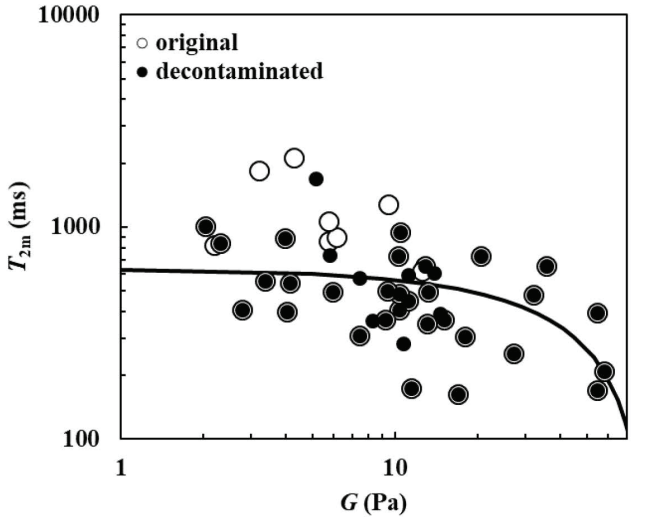

Fig. 9 – *Correlation between the sputum average relaxation time (T_{2m}) and shear modulus G (38 samples). Open circles refer to T_{2m} data not corrected for the possible saliva presence (original) while closed circles represent corrected (decontaminated) T_{2m} data. Solid line is the linear interpolant evaluated on corrected data.*

correction performed on the T_{2m} and G values. Indeed, as G was measured on whole sample, where also saliva was present, the real G value extrapolated from the network strength will be higher and it will be inversely proportional to the volume fraction occupied by the internal water. Fig. 9 shows the correlation between T_{2m} and G before (open circles) and after decontamination (closed circles). The solid line represents the interpolating straight line (T_{2m}(ms) = –7.5 ·G(Pa) + 637) evaluated on decontaminated data.

Conclusions

The focus of this paper was on the determination of the shear modulus G of sputum samples from CF patients as its knowledge, in conjunction with LF-NMR characterisation, allows 1) the determination of the mesh size distribution of the polymeric network pervading the sputum, and 2) the evaluation of the possible sputum contamination by saliva. Indeed, mesh size distribution is strictly connected to lung functionality, small mesh size being typically associated to pathological conditions. In principle, small mesh size can reduce the effect of typical drugs administered in CF therapy (e.g., mucolytics, anti-inflammatory and antibiotics) due to a hindered diffusion through the mucus and the periciliary layers. Finally, the determination of too large meshes, whose evaluation relies on G knowledge, can indicate sputum contamination by saliva.

Although the three strategies adopted for G determination (*MG*, *MG*2 and *V*) led to similar G estimations, the *MG* approach (mechanical spectrum fitting by means of the generalised Maxwell model with relaxation times scaled by a factor 10) turned out to be the best regarding that the Akaike test assigned the smallest Akaike number (*AIC*) to *MG* in 55.2 % of the samples. This is the reason why *MG* was adopted to evaluate the mesh size distribution and the possible sputum contamination by saliva. As in healthy subjects the mesh size of the polymeric network pervading the mucus is < (500–600) nm, when our strategy yielded mesh size ≥ 600 nm, the possible sputum contamination by saliva was considered and a proper decontamination strategy was defined. Importantly, this criterion served to evaluate the soundness of both the rheological and the LF-NMR approach as the mesh size distribution relies on information coming from both approaches. Data analysis revealed that contamination occurred in 21 % of the sputum studied. Interestingly, data decontamination allowed to strengthen the correlation between T_{2m} and FEV_1 suggesting the not negligible effect of sputum contamination by saliva.

CONFLICTS OF INTEREST

Authors declare no conflict of interests.

ACKNOWLEDGEMENTS

Project 2022K4Y33B – PRIN 2022 and the "Programma di valorizzazione dei brevetti del sistema universitario del Friuli Venezia Giulia" – FVG PoC, 2020, Italy, are acknowledged. GG wish to thank the Italian Ministry of Foreign Affairs and International Cooperation (project VN21GR01) for their support of the project.

References

1. *Rajendran, R. R., Banerjee, A.,* Mucus transport and distribution by steady expiration in an idealized airway geometry, Med. Eng. Phys. **66** (2019) 26. doi: https://doi.org/10.1016/j.medengphy.2019.02.006
2. *Manolidis, M., Isabey, D., Louis, B., Grotberg, J. B., Filoche, M. A.,* Macroscopic model for simulating the mucociliary clearance in a bronchial bifurcation: The role of surface tension, J. Biomed. Eng. **138** (2016). doi: https://doi.org/10.1115/1.4034507
3. *Derichs, N., Jin, B. J., Song, Y., Finkbeiner, W. E., Verkman, A. S.,* Hyperviscous airway periciliary and mucous liquid layers in cystic fibrosis measured by confocal fluorescence photobleaching, The FASEB J. Res. Commun. **25** (2011) 23. doi: https://doi.org/10.1096/fj.10-179549
4. *Button, B., Cai, L. H., Ehre, C., Kesimer, M., Hill, D. B., Sheehan, J. K., Boucher, R. C., Rubinstein, M.,* A periciliary brush promotes the lung health by separating the mucus layer from airway epithelia, SCIENCE **337** (2012). doi: https://doi.org/10.1126/science.1223012
5. *Bansil, R., Turner, B. S.,* The biology of mucus: Composition, synthesis and organization, Adv. Drug Deliv. Rev. **124** (2018) 3. doi: https://doi.org/10.1016/j.addr.2017.09.023
6. *Duncan, G. A., Jung, J., Hanes, J., Suk, J. S.,* The mucus barrier to inhaled gene therapy, Mol. Ther. **24** (2016) 2043. doi: https://doi.org/10.1038/mt.2016.182
7. *O'Sullivan, B. P., Freedman, S. D.,* Cystic fibrosis, The Lancet **373** (2009) 1891 doi: https://doi.org/10.1016/S0140-6736(09)60327-5
8. *Roger, D. F., Barnes, P. J.,* Treatment of airway mucus hypersecretion, Ann. Med. **38** (2006) 116 doi: https://doi.org/10.1080/07853890600585795
9. *Fung, C., Naughton, S., Turnbull, L., Tingpej, P., Rose, B., Arthur, J., Hu, H., Harmer, C., Harbour, C., Hassett, D. J., Whitchurch, C. B., Manos, J.,* Gene expression of *Pseudomonas aeruginosa* in a mucin-containing synthetic growth medium mimicking cystic fibrosis lung sputum, J. Med. Microbiol. **59** (2010) 1089. doi: https://doi.org/10.1099/jmm.0.019984-0
10. *Briesacher, B. A., Quittner, A. l., Fouayzi, H., Zhang, J., Swensen, A.,* Nationwide trends in the medical care costs of privately insured patients with cystic fibrosis (CF), 2001-2007, Pediatr. Pulmonol. **46** (2011) 770. doi: https://doi.org/10.1002/ppul.21441
11. *Solomon, G. M., Fu, L., Rowe, S. M., Collawn, J. F.,* The therapeutic potential of CFTR modulators for COPD and other airway diseases, Curr. Opin. Pharmacol. **34** (2017) 132. doi: https://doi.org/10.1016/j.coph.2017.09.013
12. *Zach, M. S.,* The role of recombinant human DNase in the treatment of patients with cystic fibrosis: Many promises, more problems, Thorax **51** (1996) 750. doi: https://doi.org/10.1136/thx.51.7.750
13. *Abrami, M., Maschio, M., Conese, M., Confalonieri, M., Salton, F., Gerin, F., Dapas, B., Farra, R., Adrover, A., Milcovich, G., Fornasier, C., Biasin, A., Grassi, G., Grassi, M.,* Effect of chest physiotherapy on cystic fibrosis sputum nanostructure: An experimental and theoretical approach, Drug Del. Translat. Res. **12** (2022) 1943. doi: https://doi.org/10.1007/s13346-022-01131-8
14. *Abrami, M., Maschio, M., Conese, M., Confalonieri, M., Gerin, F., Dapas, B., Farra, R., Adrover, A., Torelli, Ruaro, B., Grassi, G., Grassi, M.,* Combined use of rheology and portable low-field NMR in cystic fibrosis patients, Respir. Med. **189** (2021) 1. doi: https://doi.org/10.1016/j.rmed.2021.106623
15. *Girod, S., Zahm, J. M., Plotkowski, C., Beck, G., Puchelle, E.,* Role of the physiochemical properties of mucus in the protection of the respiratory epithelium, Eur. Respir. J. **5** (1992) 477.
16. *Flory, P. J.,* Principles of Polymer Chemistry; Cornell University Press: Ithaca, NY, USA, 1953.
17. *Schurz, J.,* Rheology of polymer solutions of the network type, Prog. Polym. Sci. **16** (1991) doi: https://doi.org/10.1016/0079-6700(91)90006-7
18. *Chui, M. M., Phillips, R. J., McCarthy, M. J.,* Measurement of the porous microstructure of hydrogels by nuclear magnetic resonance, J. Colloid Interface Sci. **174** (1995) 336.
19. *Brownstein, K. R, Tarr, C. E.,* Importance of classical diffusion in NMR studies of water in biological cells, Phys. Rev. A. **19** (1979) 2453. doi: https://doi.org/10.1103/PhysRevA.19.2446
20. *Scherer, G. W.,* Hydraulic radius and mesh size of gels, J. Sol-Gel Sci. Techn. **1** (1994) 285. doi: https://doi.org/10.1007/BF00486171
21. *Lapasin, R., Pricl, S.,* Rheology of Industrial Polysaccharides: Theory and Applications, Blackie, London, 1995.
22. *Draper, N. R., Smith, H.,* Applied regression analysis. New York: John Wiley & Sons Inc; 1966. doi: https://doi.org/10.1002/bimj.19690110613
23. *Abrami, M., Marizza, P., Zecchin, F., Bertoncin, P., Marson, D., Lapasin, R., de Riso, F., Posocco, P., Grassi, G., Grassi, M.,* Theoretical importance of PVP-alginate hydrogels structure on drug release kinetics, Gels **5** (2019) 1. doi: https://doi.org/10.3390/gels5020022
24. *Whittal, K. P., MacKay, A. L.,* Quantitative interpretation of NMR relaxation data, J. Magn. Reson. **84** (1989) 134. doi: https://doi.org/10.1016/0022-2364(89)90011-5
25. *Provencher, S. W. A.,* A constrained regularization method for inverting data represented by linear algebraic or integral equations, Comput. Phys. Comm. **27** (1982) 213. doi: https://doi.org/10.1016/0010-4655(82)90173-4
26. *Wang, X., Ni, Q.,* Determination of cortical bone porosity and pore size distribution using a low field pulsed NMR approach, J. Orthop. Res. **21** (2003) 312. doi: https://doi.org/10.1016/S0736-0266(02)00157-2
27. *Coviello, T., Matricardi, P., Alhaique, F., Farra, R., Tesei, G., Fiorentino, S., Asaro, F., Milcovich, G., Grassi, M.,* Guar gum/borax hydrogel: Rheological, low field NMR and release characterizations, eXPRESS Polym. Lett. **3** (2013) 733. doi: https://doi.org/10.3144/expresspolymlett.2013.71
28. *Abrami, M., Siviello, C., Grassi, G., Larobina, D., Grassi, M.,* Investigation on the thermal gelation of chitosan/β-glycerophosphate solutions, Carbohyd. Polym. **214** (2019) 110. doi: https://doi.org/10.1016/j.carbpol.2019.03.015
29. *Kopac, T., Abrami, M., Grassi, M., Rucigaj, A., Krajnc, M.,* Polysaccharide based hydrogels crosslink density equation: A rheological and LF-NMR study of polymer-polymer interaction, Carbohydr. Polym. **277** (2022) 1. doi: https://doi.org/10.1016/j.carbpol.2021.118895
30. *Abrami, M., Chiarappa, G., Farra, R., Grassi, G., Marizza, P., Grassi, M.*, Use of low field NMR for the characterization of gels and biological tissues, ADMET & DMPK. **6** (2018) 34. doi: https://doi.org/10.5599/admet.6.1.430.
31. *Holz, M., Heil, S. R., Sacco, A.*, Temperature-dependent self-diffusion coefficients of water and six selected molecular liquids for calibration in accurate 1H NMR PFG measurements, Phys. Chem. Chem. Phys. **2** (2000) 4740. doi: https://doi.org/10.1039/B005319H

32. *Meiboom, S., Gill, D.,* Modified spin-echo method for measuring nuclear relaxation times, Rev. Sci. Instrum. **29** (1958) 688. doi: https://doi.org/10.1063/1.1716296
33. *Baumgaertel, M., Winter, H. H.,* Determination of discrete relaxation and retardation time spectra from dynamic mechanical data, Rheol. Acta **28** (1989) 511. doi: https://doi.org/10.1007/BF01332922
34. *Winter, H. H.,* Analysis of dynamical mechanical data: Inversion into a relaxation time spectrum and consistency check, J. Non-Newtonian Fluid Mech. **68** (1997) 225 doi: https://doi.org/10.1016/S0377-0257(96)01512-1
35. *Jensen, E. A.,* Determination of discrete relaxation spectra using Simulated Annealing, J. Non-Newtonian Fluid Mech. **107** (2002) 1. doi: https://doi.org/10.1016/S0377-0257(02)00110-6
36. *Monaco, F. J., Delbem, A. C. B., Federson, F. M.,* Genetic algorithm for the determination of linear viscoelastic relaxation spectrum from experimental data, J. Appl. Polym. Sci. **113** (2009) 122. doi: https://doi.org/10.1002/app.29496
37. *Stadler, F. J., Christian Bailly, C.,* A new method for the calculation of continuous relaxation spectra from dynamic-mechanical data, Rheol. Acta **48** (2009) 33. doi: https://doi.org/10.1007/s00397-008-0303-2
38. *Takeh, A., Shanbhag, S.,* A computer program to extract the continuous and discrete relaxation spectra from dynamic viscoelastic measurements, Appl. Rheol. **23** (2013) 24628. doi: https://doi.org/10.3933/applrheol-23-24628
39. *Dacol, V., Caetano, E., Correia, J. R.,* A new viscoelasticity dynamic fitting method applied for polymeric and polymer-based composite materials, Materials **13** (2020) 5213. doi: https://doi.org/10.3390/ma13225213
40. *Abrami, M., Ascenzioni, F., Di Domenico, E. G., Maschio, M., Ventura, A., Confalonieri, M., Digioia, G. S., Conese, M., Dapas, B., Grassi, G., Grassi, M.,* A novel approach based on low-field NMR for the detection of the pathological components of sputum in cystic fibrosis patients, Magn. Reson. Med. **79** (2018) 2323. doi: https://doi.org/10.1002/mrm.26876
41. *Motulsky, H., Christopoulos, A.,* Fitting models to biological data using linear and non linear regression. GraphPad Prism Manual, version 4.0 (2003) chapter 23.
42. *Mezzasalma, S. A., Abrami, M., Grassi, G., Grassi, M.,* Rubber elasticity of polymer networks in explicitly non-Gaussian states. Statistical mechanics and LF-NMR inquiry in hydrogel systems, Int. J. Eng. Sci. **176** (2022) 1. doi: https://doi.org/10.1016/j.ijengsci.2022.103676
43. *Abrami, M., Maschio, M., Conese, M., Confalonieri, M., Di Gioia, G. S., Gerin, F., Dapas, B., Tonon, F., Farra, R., Murano, E., Zanella, G., Salton, F., Torelli, L., Grassi, G., Grassi, M.,* Use of low field nuclear magnetic resonance to monitor lung inflammation and the amount of pathological components in the sputum of cystic fibrosis patients, Magn. Reson. Med. **84** (2020) 427. doi: https://doi.org/10.3390/ijerph18094691
44. *Suk, J. S., Lai, S. K., Wang, Y. Y., Ensign, L. M., Zeitlin, P. L., Boyle, M. P., Hanes, J.,* The penetration of fresh undiluted sputum expectorated by cystic fibrosis patients by non-adhesive polymer nanoparticles, Biomaterials **30** (2009) 2591. doi: https://doi.org/10.1016/j.biomaterials.2008.12.076
45. *Suk, J. S., Lai, S. K., Boylan, N. J., Dawson, M. R., Boyle, M. P., Hanes, J.,* Rapid transport of mucoinert nanoparticles in cystic fibrosis sputum treated with N-acetyl cysteine, Nanomedicine **6** (2011) 365. doi: https://doi.org/10.2217/nnm.10.123
46. *Michael, A., Zhou, Y. N., Yavuz, M., Khan, M. I.,* Deconvolution of overlapping peaks from differential scanning calorimetry analysis for multi-phase NiTi alloys, Thermochimica Acta **665** (2018) 53. doi: https://doi.org/10.1016/j.tca.2018.05.014
47. *Turco, G., Donati, I., Grassi, M., Marchioli, G., Lapasin, R., Paoletti, S.*, Mechanical spectroscopy and relaxometry on alginate hydrogels: A comparative analysis for structural characterization and network mesh size determination, Biomacromolecules **12** (2011) 1272. doi: https://doi.org/10.1021/bm101556m
48. *Schuster, B. S., Suk, J. S., Woodworth, G. F., Hanes, J.,* Nanoparticle diffusion in respiratory mucus from humans without lung disease, Biomaterials **34** (2013) 3439. doi: https://doi.org/10.1016/j.biomaterials.2013.01.064
49. Standards for the clinical care of children and adults with cystic fibrosis in the UK. London: UK Cystic Fibrosis Trust. 2011.
50. *Ponce, M. C., Sankari, A., Sharma, S.,* StatPearls [Internet]. StatPearls Publishing; Treasure Island (FL): (2022). Pulmonary Function Tests.
51. *Matarese, A., Sardu, C., Shu, J., Santulli, G.,* Why is chronic obstructive pulmonary disease linked to atrial fibrillation? A systematic overview of the underlying mechanisms, Int. J. Cardiol. **276** (2019) 149. doi: https://doi.org/10.1016/j.ijcard.2018.10.075
52. *Zakaria, R., Harif, N., Al-Rahbi, B., Aziz, C. B. A., Ahmad, A. H.,* Gender differences and obesity influence on pulmonary function parameters, Oman Med. J. **34** (2019) 44. doi: https://doi.org/10.5001/omj.2019.07
53. *Gao, C., Zhang, X., Wang, D., Wang, Z., Li, J., Li, Z.,* Reference values for lung function screening in 10- to 81-year-old, healthy, never-smoking residents of Southeast China, Medicine (Baltimore) **97** (2018) e11904. doi: https://doi.org/10.1097/MD.0000000000011904
54. *Shapira, U., Krubiner, M., Ehrenwald, M., Shapira, I., Zeltser, D., Berliner, S., Rogowski, O., Shenhar-Tsarfaty, S., Bar-Shai, A.,* Eosinophil levels predict lung function deterioration in apparently healthy individuals, Int. J. Chron. Obstruct. Pulmon. Dis. **14** (2019) 597. doi: https://doi.org/10.2147/COPD.S192594